

A mathematical model and numerical simulation for SARS-CoV-2 dynamics

Antonino Amoddeo (✉ antonino.amoddeo@unirc.it)

Università 'Mediterranea' di Reggio Calabria

Article

Keywords:

Posted Date: May 26th, 2022

DOI: <https://doi.org/10.21203/rs.3.rs-1662358/v1>

License:  This work is licensed under a Creative Commons Attribution 4.0 International License.

[Read Full License](#)

A mathematical model and numerical simulation for SARS-CoV-2 dynamics

Antonino Amoddeo

Department of Civil, Energy, Environment and Materials Engineering, Università 'Mediterranea' di Reggio Calabria, Via Graziella 1, Feo di Vito, I-89122 Reggio Calabria, Italy
antonino.amoddeo@unirc.it; Tel: +39-0965-169-3299; Fax: +39-0965-169-22201.

ABSTRACT

Since its outbreak the corona virus -19 disease has been particularly aggressive for the lower respiratory tract, and lungs in particular. The dynamics of the abnormal immune response leading to lung damage with fatal outcomes is not yet fully understood. We present a mathematical model describing the dynamics of corona virus disease - 19 starting from virus seeding inside the human respiratory tract, taking into account its interaction with the components of the innate immune system as classically and alternatively activated macrophages, interleukin-6 and -10. The numerical simulations have been performed for two different parameter values related to the pro-inflammatory interleukin, searching for a correlation among components dynamics during the early stage of infection, in particular pro- and anti-inflammatory polarizations of the immune response. We found that in the initial stage of infection the immune machinery is unable to stop or weaken the virus progression. Also an abnormal anti-inflammatory interleukin response is predicted, induced by the disease progression and clinically associated to tissue damages. The numerical results well reproduce experimental results found in literature.

Introduction

The Severe Acute Respiratory Syndrome (SARS) - Corona Virus-2 (CoV-2) appeared at the end of 2019, and can be responsible for a severe inflammation of the human respiratory tract (HRT), a disease also known as Corona Virus Disease - 2019 (COVID-19): it is characterized by an abnormal response of the immune system which induces the production of several inflammatory molecules going in circulations and giving rise to a so-called cytokine storm^{1,2}, an event with outcome often lethal, and whose occurrence is shared with previous coronaviruses such as SARS-CoV and Middle East Respiratory Syndrome (MERS)-CoV^{2,3}.

In general, upon infection, the host response begins with the detection of the pathogen associated molecular patterns (PAMP) through the pattern recognition receptors (PRR), allowing the recognition of the external pathogen and leukocytes activation, then triggering the response of the innate immunity^{1,4}. This is the first source of inflammation as response of the host to the pathogen exposure. At the same time the innate immune system, which includes monocytes, macrophages, dendritic cells, mast cells, natural killer cells, neutrophils, eosinophils and basophils, represents the first barrier of the host opposing to an external thread. Since the outbreak of the COVID-19, works have put in evidence the peculiarity of the disease as well the similarities with SARS-CoV, MERS-CoV^{2,5}, while previous studies and mathematical models⁶⁻⁹ can be a foundation from which to build a mathematical modelling for SARS-CoV-2 infection. In this work we are concerned with a mathematical model trying to shed some light on the COVID-19 dynamics during the early stage of the disease progression, taking into account the virus interaction with the host innate immune response. We summarize the essential biological background needed for the model presentation and

discussion, while for more details as well as review papers it is very difficult to select among a wealth of excellent ones which are present in literature, then we address the interested reader to papers cited time to time and references therein.

When a pathogen intrudes a host, it is faced by monocytes, which consequently differentiate into macrophage (M) or dendritic cell (DC)¹⁰. Such cells, once captured the pathogen, interact with T lymphocytes, which in turn are grouped into four types of population, among which there is the family of the effector T lymphocytes: the latter includes cytotoxic T-lymphocytes or CD8⁺ T-cells, regulators T-lymphocytes or T_{reg} cells, and helper T-lymphocytes or CD4⁺ T-cells¹¹. Cytokines, a broad class of peptides that includes chemokines (CK) and interleukins (IL)¹, are important mediator of the immune response and play a significant role in cell signalling and activation of the immune response^{12,13}.

Once activated as a consequence of an external threat, CD4⁺ T-cells start producing a variety of ILs¹² that are responsible of the cell signalling, producing a broad immune response.

Macrophages differentiate from monocytes in classically activated macrophages (M1), or in alternatively activated macrophages (M2)^{4,14-16}. The former are associated to a pro-inflammatory activity since they produce pro inflammatory ILs as, for example in tumour progression¹⁷: tumour necrosis factor (TNF), IL-1, IL-6 and IL-12. On the other hand, M2 macrophages are responsible of an anti-inflammatory activity since they produce anti-inflammatory ILs, such as IL-10, and perform a restorative and healing function for damaged cells¹⁸.

ILs are molecules that can exert both pro- and anti-inflammatory functions^{13,19} and are produced not only by macrophages, but also by CD4⁺-T cells. Pro-inflammatory ILs are produced by M1 activated macrophages, and high levels of in particular IL-6 are present in severe COVID-19 patients, as well in SARS and MERS ones². In a very recent review²⁰ the immunoregulatory role of IL-10 in many infections has been summarized, while it has been found that IL-10 secreted in the tumour environment encourage differentiation towards the M2 phenotype²¹.

In Lai *et al.*⁷ a model for the dynamics of CD8⁺ T cells during Human Immunodeficiency Virus (HIV) -1 infection at a quasi steady state has been presented, considering contributions from both healthy and infected CD4⁺ T cells, and introducing a chemotactic contribution due to infected CD4⁺ T cells. It is found that the steady state stability depends upon attractive or repulsive nature of the chemotactic movement²².

In a recent work of Quirouette *et al.*⁸, the spread of influenza A virus (IAV) in the HRT has been modelled in terms of partial differential equations (PDEs), considering diffusion and advection terms in one spatial dimension as well the interaction of virions with both healthy and infected target cells. Models formulated in term of ordinary differential equations (ODE) have been constructed for Dengue Virus (DV) spread coupled with the immune response²³, while a review for the viral dynamics of HIV, Hepatitis C Virus (HCV), IAV, Ebola Virus (EV), DV and Zika Virus (ZV) has been presented in Zitzmann & Kaderali⁶.

Less recently, a model describing the space-time evolution of cancer cells has been formulated in terms of PDEs, taking into account their interaction with CD8⁺-T cells, IL-27, IL-10 and interferon- γ (INF- γ)⁹, in one spatial dimension, highlighting the role of pro- and anti-inflammatory ILs.

At the turn of the pandemic declaration of the World Health Organization, a couple of paper reported clinical results of studies carried out on COVID-19 patients in Wuhan, China, in which the plasma levels of IL-6 and IL-10²⁴, and of IL-6²⁵ were measured. In this frame, the present work is aimed at: (1) investigate a possible IL-6 role on M1 polarization of macrophages while they undergo chemotaxis from SARS-CoV-2 infected T cells; hence, (2) reproduce clinical observations

on SARS-CoV-2 patients, linked to the dynamics of ILs and the role they play in lung damages. To build our model we were inspired by the works of Chousterman *et al.*¹, Rossi *et al.*², Channappanavar *et al.*³, while the numerical simulations were compared with clinical findings contained in Huang *et al.*²⁴, Zhou *et al.*²⁵, taking some points of discussion and comparison also from previous experimental works on mice^{26,27}.

The mathematical model

We consider a portion of the HRT as the domain in which an initial amount of virus (V) explicitly interacts with CD4⁺-T cells, from now on simply T cells, and in which the immune response involves classically ($M1$) and alternatively ($M2$) activated macrophages, IL-6 (L) and IL-10 (N). From the mass conservation we derive the model equations for the interacting species inside the considered biological domain, in terms of reaction-diffusion PDEs. We consider the spatial position identified by the vector $\mathbf{x} = (x,y)$, while t denotes the variable time.

We therefore introduce the relative model equations, together with a model equation accounting for infected T cells (I). Once SARS-CoV-2 intrudes the host, it binds to angiotensin-converting enzyme 2 (ACE2) receptors²⁵, subsequently its presence is revealed by the toll-like receptors (TLR) from which the immune response begins with the associated inflammation². ACE2 have been proven to be the receptors of SARS-CoV and SARS-Cov-2^{11,28}, both targeting T cells, a characteristics shared with HIV-1^{7,29}. Then considering only infection of such cells, the virus evolution accounts for diffusion with a coefficient D_V , production by I cells at a rate p ; the virus is cleared by immune elimination⁶ at a rate c :

$$\frac{\partial V}{\partial t} = \nabla \cdot (D_V \nabla V) + pI - cV \quad . \quad (1)$$

T cells diffuse at rate D_T , undergo natural decay according to d_T , and are infected by virus at rate $k^{6,7}$; are activated by $L^{30,31}$, promoted by $M1^{10}$, inhibited by $N^{20,32,33}$ and $M2^{10}$ according to ϕ_{21} , ϕ_{22} , ϕ_{23} and ϕ_{24} , respectively.

$M1$ produce, among others, IL-12 driving T cell polarization³⁴; the presence in the airways inflammatory microenvironment of IL-4 and IL-13 induce $M2$ polarization of macrophages³⁵, in turn expressing N which increases T cell deactivation. On the other hand T_{reg} cells, which differentiation is stimulated by N , inhibit T cell and DC activation^{35,36}. In the lung, T_{reg} are promoted by alveolar macrophages, with a predominant $M2$ phenotype³⁷. Given the common features evidenced, for example, in Mannar *et al.*³⁸ and Fardos *et al.*³⁹ between SARS-CoV-2 and HIV-1, along with the fact that T cells are decreased in critical COVID-19 patients⁴⁰, we suppose that, similarly to what happens for HIV-1^{7,22,41}, depending on the concentration of some CKs, in presence of the SARS-CoV-2 infection, T cells undergo chemoattraction (chemotaxis) or chemorepulsion (fugetaxis). We then assume that T cells are attracted towards I cells, but are repulsed by virions, allowing SARS-CoV-2 immune evasion. In equation (2), χ_I and χ_V are, respectively, chemotaxis and fugetaxis coefficients for T cells; T_M , instead, represents the maximum carrying capacity of T population.

$$\frac{\partial T}{\partial t} = \nabla \cdot \left\{ D_T \nabla T - T \left[\chi_I \left(1 - \frac{T}{T_M} \right) \nabla I - \chi_V \left(1 - \frac{T}{T_M} \right) \nabla V \right] \right\} - d_T T - kVT + \phi_{21}L + \phi_{22}M_1 - \phi_{23}N - \phi_{24}M_2 \quad (2)$$

I cell are supposed to diffuse at the same rate of T cell; they are produced by the V - T interaction at rate k , and decay at rate δ ; it is also conceivable that the I - L interaction can promote activation of effector T cells and deactivation of T_{reg} cells²⁷, contributing to an hyper-inflammation further reducing I at rate ϕ_{32} :

$$\frac{\partial I}{\partial t} = \nabla \cdot (D_T \nabla I) + kVT - \delta I - \phi_{32}IL \quad (3)$$

Classically activated macrophages diffuse according to D_{M1} . High levels of pro-inflammatory ILs, in particular L , characterize the biological milieu of the SARS-CoV-2 infection^{1,2}. From one hand it can be hypothesized that, similarly to what happens in chronic wounds, where the shift from $M1$ to $M2$ phenotype is dis-regulated with a prolonged inflammatory state¹⁴, a persistence of $M1$ macrophages and their predominance over $M2$ phenotypes can occur. On the other side, in Hadjadj *et al.*⁴² it has been found that in severe and critical COVID-19 patients an excessive inflammatory response occurs with increased levels of IL-6 which can act as a chemoattractant for macrophages and consequent tissue damage. Moreover, in COVID-19 patients an extreme increase of pro-inflammatory cytokines and other factors has been observed, among which IL-6 and IFN- γ ⁴³. Therefore, although in the literature we have not found evidence that L induces or promotes $M1$ directly, due to the peculiarity of the SARS-CoV-2 infection we assume that the abnormal expression of L and IFN- γ promotes $M1$ at a rate ϕ_{41} . Further, the inflammation resolution involves the release of anti-inflammatory ILs^{18,20,21}, then $M1$ are inhibited by N at rate ϕ_{42} .

In critical COVID-19 patients a common feature is that in lung lesions the predominant infiltrated immune cells are constituted by monocytes and macrophages^{28,40}. The deeper penetration in tumour lesions of $M1$ macrophages with respect to $M2$ subtypes has been simulated in Leonard *et al.*¹⁷, Mahlbacher *et al.*²¹, accounted for introducing a chemotactic movement towards the lesion. The macrophage chemotaxis has been introduced also in Owen *et al.*⁴⁴, studying macrophages-based therapies for drug delivery to tumour sites. $M1$ phenotype predominates in the early stage of inflammation and wound repair¹⁴, with a shift from $M1$ to $M2$ within 5-7 days post injury, being such behaviour dis-regulated in presence of chronic wounds. Given the pro-inflammatory nature of $M1$ macrophages, we then assume that they move chemotactically towards infected cells according a chemotactic coefficient χ_I :

$$\frac{\partial M_1}{\partial t} = \nabla \cdot \left[D_{M1} \nabla M_1 - M_1 \chi_I \left(1 - \frac{M_1}{M_{1M}} \right) \nabla I \right] + \phi_{41}L - \phi_{42}N \quad , \quad (4)$$

where M_{1M} is the maximum carrying capacity of $M1$ population.

Alternatively activated macrophages $M2$ diffuse at rate D_{M2} , and are promoted by N , which induce macrophages differentiation towards $M2$ ^{2,21} at a rate ϕ_{51} ; the spike protein in SARS-CoV-2 is

responsible of hyper production of IL-6⁴⁵, and in general of a complicated frame of hyper-inflammation leading to the cytokine storm, but also excess of IFN- γ has been observed⁴³. We assume here that the level of L is representative of inflammation and therefore reflects proportionally that of IFN- γ , which in turn can repolarize $M2$ macrophages towards $M1$ phenotype⁴⁶. Hence, $M2$ are inhibited at rate ϕ_{52} according to the L increase:

$$\frac{\partial M_2}{\partial t} = \nabla \cdot (D_{M_2} \nabla M_2) + \phi_{51} N - \phi_{52} L \quad . \quad (5)$$

L diffuses at rate D_L , it is produced by $M1$ at rate ϕ_{61} ^{1,10,14,17}; on the other hand, L is inhibited by N at rate ϕ_{63} ^{1,20,21,47}:

$$\frac{\partial L}{\partial t} = \nabla \cdot (D_L \nabla L) + \phi_{61} M_1 - \phi_{63} N \quad . \quad (6)$$

Finally, N diffuses at rate D_N , is produced by $M2$ macrophages at rate ϕ_{71} ^{14,20}, while it is inhibited by L at rate ϕ_{73} ¹:

$$\frac{\partial N}{\partial t} = \nabla \cdot (D_N \nabla N) + \phi_{71} M_2 - \phi_{73} L \quad . \quad (7)$$

Methods

We performed numerical simulations of the above PDE system using the COMSOL MultiphysicsTM package based on the finite element method (FEM)⁴⁸, referring to the supplementary material for details. In equation (2) and equation (4), we set $T_M = T_r$ and $MI_M = MI_r$, respectively, where T_r and MI_r are reference quantities: Table 1 groups all the used parameters in dimensional and non-dimensional form, together with a short description and estimate, while once again we refer to the supplemental material for details and used sources.

Equations (1)-(7) have been integrated in a two-dimensional squared domain with 1mm^2 area, simulating a surface of HRT, in the 0-60 non-dimensional time interval. At $t = 0$ we assume the following set of initial conditions:

$$\begin{aligned} V(\mathbf{x},0) &= \exp(-|\mathbf{x}|^2 \varepsilon^{-1}) \\ T(\mathbf{x},0) &= 1 - 0.5V(\mathbf{x},0) \\ I(\mathbf{x},0) &= 0.5V(\mathbf{x},0) \\ MI(\mathbf{x},0) &= 0.05V(\mathbf{x},0) \\ M2(\mathbf{x},0) &= 0.1 \exp(-|\mathbf{x}|^2 \varepsilon^{-1}) \\ L(\mathbf{x},0) &= 0.05V(\mathbf{x},0) \\ N(\mathbf{x},0) &= 0 \end{aligned} \quad (8)$$

In the above equations $\varepsilon = 0.02$, then we admit that the initial viral load is centred on $\mathbf{x} = (0,0)$ with Gaussian shape. Moreover, a fraction of T cells is initially infected, while the MI activated

macrophages are a small fraction of the viral load. At $t = 0$ the $M2$ activation is not yet started then we assume that a Gaussian distribution of alternatively activated macrophages is centred at $\mathbf{x} = (0,0)$, L is produced according to the $M1$ macrophages while N is not yet produced by $M2$. During the simulations the model has been tested for robustness by allowing each parameter to vary within $\pm 10\%$ of the selected value, with no significant changes observed in the virus amount in the domain at $t = 60$. Instead, the numerical simulations have been performed as a function of the ϕ_{52} parameter, in order to test the biological milieu change capable to polarize macrophages towards $M1$ or $M2$ phenotype⁴⁶, and for this reason we imposed $\phi_{52} = 1 \times 10^{-3}, 2 \times 10^{-3}$.

Results and Discussion

We performed the numerical simulation of equations (1)-(7), plotting the variables spatial distribution for selected time steps in colour scale between the blue (minimum) and the red (maximum), which at $t = 0$ obey to the initial conditions imposed with equations (8). Moreover, each variable distribution has been normalized to its maximum value assumed during the time evolution. The variables evolution has been computed at $t = 10$ (~1.16 days), $t = 20$ (~2.3 days), $t = 30$ (~3.47 days), $t = 40$ (~4.63 days), $t = 50$ (~5.79 days) and $t = 60$ (~6.94 days). We start showing in Fig. 1 the V dynamics inside the simulated domain, for $\phi_{52} = 1 \times 10^{-3}$ (first column) and $\phi_{52} = 2 \times 10^{-3}$ (second column). On going from $t = 10$ to $t = 40$ no features can apparently be observed, because of the damping due to the intensity normalization. At $t = 50$ the growing virus spatial distribution becomes visible as it has invaded almost half of the domain, while at $t = 60$ it has spread over the entire domain. No appreciable differences can be noted depending on the ϕ_{52} values. As expected, directly correlated to the virus dynamics is that of I cell, as shown in Supplementary Fig. S1 online. The dynamical evolution of the T cells is shown in Fig. 2: they progressively invade the domain as a spherical wave propagating from the origin up to $t = 40$; at $t = 50$ the primary front decreases while a secondary one starts to form, well visible at $t = 60$, insensitive to ϕ_{52} values. The $M1$ evolution is shown in Supplementary Fig. S2 online, damped and visible only close to the origin due to the intensity normalization, and for both ϕ_{52} values decreases up to $t = 40$, slightly growing from $t = 50$ on. More pronounced, instead, appears the density variation of the alternatively activated macrophages $M2$, which dynamical evolution is shown in Supplementary Fig. S3 online: for both ϕ_{52} values $M2$ density grows progressively across the domain starting from the initial cluster at the origin, which close to the origin initially decrease up to $t = 40$, then from $t = 50$ increases again.

The L dynamics, see Supplementary Fig. S4 online, grows without appreciable differences for both ϕ_{52} values until $t = 40$, while the intensity at the origin remain almost unchanged during the propagation across the domain, then slightly decreases.

The N dynamical evolution shown in Supplementary Fig. S5 online, instead, appears more defined and seems a little faster for the lower ϕ_{52} value, and exhibits a monotonic growth.

The computed densities shown in Figs. 1-2 and in Supplementary Figs. S1-S5 online, have been integrated in order to obtain, at each time step, the total amount of each species present in the domain, and the results are shown in Fig. 3, except for I cells which total quantity is shown in Supplementary Fig. S6 online. First of all, the plots put in evidence the small differences existing between the quantities of each species present in the domain as a function of the ϕ_{52} value, sometimes not even graphically resolved. The virus amount present in the domain grows

progressively as a function of time, and increases dramatically above $t = 50$, while I cells behave very similarly. T cells increases up to $t = 50$, then start decreasing, and very similarly behave also held $M1$ macrophages. L grows during the time evolution but reaches a maximum at $t = 40$, and then dramatically decrease up to $t = 60$. Both $M2$ macrophages and N behave very similarly to V , and unexpectedly assume also very close values. As expected, it can be said that anti-inflammatory contributions should be promoted at low ϕ_{52} values, and *vice versa* for pro-inflammatory ones. These results are consistent from a biological point of view, as $M1$ macrophages induce T cells activation and L production, while activated $M2$ macrophages induce N production.

In order to gain more insights on the density spatial distribution, we extract the density profiles for each species along the diagonal line cutting the 2D density maps, hence the domain, from $(x_1 = 0, y_1 = 0)$ to $(x_2 = 1, y_2 = 1)$, from now on referred to as the diagonal cutline, i.e., along the line splitting each density plot into two symmetric domains with respect the diagonal line. In Fig. 4 we show the cross-sectional densities of the V , T and I cells. The plots referring to V and to I cells are very similar, as they reflect those of Fig. 1 and Supplementary Fig. S1 online, respectively, and show a growing density from $t = 10$ to $t = 60$, quite insensitive to the ϕ_{52} values. The cross-sectional density for T cells, instead, shows a predominant cells redistribution: in fact, starting from a huge peak located around the origin at $t = 10$, during the time evolution such feature decreases while broadening, and at $t = 60$ a new peak arises located along the diagonal cut-line at about $r = 0.9$ (0.9 mm), consistent with the secondary propagation front visible in Fig. 2.

Following the same graphical format of the previous 1D plots, we choose to group the cross-sectional densities for macrophages and interleukins in Fig. 5 and Fig. 6, respectively. The peak in the density of $M1$ phenotype around $r = 0$ decreases up to $t = 40$, then increases again from $t = 50$, indifferently for both ϕ_{52} values, see Fig. 5. The $M2$ density peak centred at $r = 0$ decreases progressively up to $t = 40$ as it widens, while increases again for $t = 50$ and $t = 60$, superimposed on a growing background indicating the penetration of the cells into the domain. Such behaviour for $M2$ cells seems to be more defined at $\phi_{52} = 1 \times 10^{-3}$, as measured by the density peak at $r = 0$. Concerning interleukins, Fig. 6, it is evident as the L maximum intensity at $r = 0$ does not change on going from $t = 10$ to $t = 60$ along the diagonal cut-line, but a background rises progressively up to $t = 40$, while at $t = 60$ it flattens towards zero. On the contrary, the N density grows progressively while infiltrating the domain, and starting from $t = 40$ does it faster for $\phi_{52} = 1 \times 10^{-3}$.

According to what reported in Channapanavar *et al.*³, in patients with fatal SARS and MERS the lower respiratory tract is involved, with experimental evidences of lung infiltration by monocytes/macrophages, and low counts of CD4 T cells. Our model describes such feature adequately. In fact, as can be seen in Fig. 4, during the time evolution T cells cross-sectional density decreases in the seeding site redistributing in space with low proliferation and equally low infiltration of the simulated domain, except the weak secondary peak. At the same time, $M2$ macrophages, but not $M1$ phenotype, for $r > 0$ progressively infiltrate in the biological domain. Nicholls *et al.*⁴⁹ and Gu *et al.*⁵⁰ from one side, and Ng *et al.*⁵¹ from the other, reported lung infiltration by macrophages from autopsy samples in patients with fatal SARS and MERS, respectively. In both cases the identification of the macrophages was conducted by means of CD68 marker, a glycoprotein highly expressed by macrophages, and in particular by $M2$ phenotypes, which characterize an anti-inflammatory and immunosuppressive micro-environment⁵². In light of these considerations we deduce that, although our model incorporates a chemotaxis term for $M1$ macrophages, it describes a macrophages dynamics with $M2$ subtypes infiltrating the domain faster

with respect to *M1* subtypes. Also, the immunosuppressive and anti-inflammatory microenvironment as determined by the *M2* predominance explains the low count of *T* cells as predicted by the model and reported by experimental findings in SARS and MERS patients⁴⁹⁻⁵¹. Du *et al.*²⁶ studied the regulatory effects on macrophages of cannabinoid 2 receptor (CB2R) during incised skin wound healing in mice: they measured the levels of mRNA of *M1* and *M2* macrophages activated markers, as well the levels of pro- and anti-inflammatory cytokines, IL-6 and IL-10 among others, in mice treated with JWH133, GP1a CB2R agonist and AM630 CB2R antagonist, which were compared to the results obtained on a vehicle group. Focusing on those latter, it can be seen as *M1* macrophages increase in content up to three days from the wound, then decrease; a similar behaviour is observed for *M2* subtypes, which initially increases at a low rate, and then accelerates thus demonstrating the initial predominance of the *M1* activated subtypes. The *M2* content peaks 5 days post injury, then slightly decreases, still remaining higher than *M1* subtypes. Overall, the content of both macrophages subtypes varies in the same range. Concerning our predictions, as shown in Fig. 3, they are in part in agreement, although delayed, with the findings of Du *et al.*²⁶, considering their reported experimental error. In fact, the *M1* content grows up to 5.79 days ($t = 50$), and then decreases; on the contrary, the content of *M2* macrophages increases monotonically, soon overwhelming the *M1* one. Concerning the IL-6 and IL-10 content in Du *et al.*²⁶, they reflect the behaviour of *M1* and *M2*, respectively, and once again, their variation is contained within the same order of magnitude. Also in our simulation *L* and *N* contents reflect *M1* and *M2* behaviour, but *N* content, compared to that of *L*, has a variation an order of magnitude larger.

Huang *et al.*²⁴ measured the initial plasma level of, among other, IL-6 and IL-10, in COVID-19 patients from Intensive Care Unit (ICU), non-ICU patients and healthy ones, on admission to hospitalization seven days after the onset of illness. In both ICU and non-ICU patients elevated level of both interleukins, with a predominance of IL-10 in ICU patients, were found. Further, Zhou *et al.*²⁵ measured the dynamics of several laboratory markers including IL-6 in COVID-19 patients, survivors or with fatal outcome. Their findings, in the 4-7 days temporal range from the illness onset, are in qualitative agreement with the predictions of our model, considering the reported experimental error.

Curiously, comparing the *M2* and *N* contents in Fig. 3, they appear to be overlapping within the graphic resolution. The plots refer to the total protein amount at each time step, so we wonder if a similar correspondence can be found in the density spatial distribution during the time evolution. The answer is in Fig. 5 and Fig. 6, for *M2* and *N* cross sectional densities along the diagonal cut-line, respectively. *M2* are initially clustered in the site of infection, and during the time evolution their density decreases and broadens while infiltrating the domain, thus indicating an initial depletion at the infection site, always predominating over *M1*, see Fig. 5. The *N* level, instead, is initially lower with respect to *L*, but from the site of infection it grows continuously while infiltrating the domain, overwhelming the *L* density. Then, even if the total amount of both *M2* and *N* species are strictly comparable at each time step, their spatial distribution are not, therefore indicating different, albeit correlated, dynamics. Globally, the simulations results confirm that the initial stage of infection is characterized by a pro-inflammatory response that during the time evolution dims in favour of the anti-inflammatory reaction. While the inflammatory response is entrusted to *M1* and *L*, the anti-inflammatory reaction instead relies on *M2* and *N*, but during the initial stage of infection it is driven mainly by *M2* and confined near the infection site. Longhi *et al.*²⁷ carried out experiments on influenza A infected mice assessing the role of IL-6 in

limiting the activity of T_{reg} cells. In particular, they measured the number of $CD4^+$ -T cells in lung, both primary and memory (after re-infection), in wild type and IL-6 deprived mice. It can be observed as the predicted quantity of T cell shown in Fig. 3 well reproduce the measurements for memory $CD4^+$ -T cells in IL-6 deprived mice reported in Longhi *et al.*²⁷, for the corresponding time interval. It can be deduced that SARS-CoV-2 infection impairs T cells response as in an L deprived environment.

It seems that our model, accounting for SARS-CoV-2 infection, predict some resistance to the immune machinery, as indeed the experimental results in Huang *et al.*²⁴, and in Zhou *et al.*²⁵ indicate. In fact, in presence of a wound healing triggered by a surgical incision²⁶, the M1 behaviour is consistent with their inflammatory role during the first stage post injury, while M2 behave consistently to their anti inflammatory and repairing role post inflammation. In our study, in the presence of a severe infection such as that caused by SARS-CoV-2, both $M1$ and L drive the inflammatory response, although with some delay with respect to the initial insult. The infection grows progressively in the simulated time interval, apparently unaffected by the immune response: we observe that the inflammatory response weakens, while the anti-inflammatory response is strengthened, precisely when viral production increases. Moreover, what it seems wrong in the immune machinery is the anti-inflammatory reaction with an excess of $M2$ activation and N production, which could eventually lead to a damage of the respiratory tract interested by the infection, i.e. pulmonary fibrosis²⁶.

The proposed model aimed at describing the COVID-19 dynamics is consistent and in qualitative agreement with clinical observations in severe COVID-19 patients. It therefore constitutes a baseline from which to start including models aimed at treatments and possible therapeutic strategies.

Data Availability Statement

All data generated or analysed during this study are included in this published article (and its supplementary information files).

References

1. Chousterman, B.G., Swirski, F.K. & Weber, G.F. Cytokine storm and sepsis disease pathogenesis. *Semin. Immunopathol.* **39**, 517–528 (2017).
2. Rossi, F., Tortora, C., Argenziano, M., Di Paola, A. & Punzo F. Cannabinoid receptor type 2: a possible target in SARS-CoV-2 (CoV-19) infection? *Int. J. Mol. Sci.* **21**, 3809; doi:10.3390/ijms21113809 (2020).
3. Channappanavar, R. & Perlman, S. Pathogenic human coronavirus infections: causes and consequences of cytokine storm and immunopathology. *Semin. Immunopathol.* **39**, 529–539 (2017).
4. Snyder, R.J. *et al.* Macrophages: a review of their role in wound healing and their therapeutic use. *Wound Repair. Regen.* **24**, 613–629 (2016).
5. Petrosillo, N., Viceconte, G., Ergonul, O., Ippolito, G. & Petersen E. *COVID-19, SARS and MERS: are they closely related?* *Clin. Microbiol. Infect.* **26**, 729-734; doi:10.1016/j.cmi.2020.03.026 (2020).
6. Zitzmann, C. & Kaderali L. Mathematical analysis of viral replication dynamics and antiviral treatment strategies: from basic models to age-based multi-scale modeling. *Front. Microbiol.* **9**, 1546; doi: 10.3389/fmicb.2018.01546 (2018).
7. Lai, X. & Zou X. A reaction diffusion system modeling virus dynamics and CTL response with chemotaxis. *Disc. Cont. Dyn. Syst. B* **21**, 2567-2585; doi: 10.3934/dcdsb.2016061 (2016).
8. Quirouette, C., Younis, N.P., Reddy, M.B. & Beauchemin, C.A.A. A mathematical model describing the localization and spread of influenza A virus infection within the human respiratory tract. *PLoS Comput. Biol.* **16**, e1007705; <https://doi.org/10.1371/journal.pcbi.1007705> (2020).
9. Liao, K.L., Bai, X.F. & Friedman A. Mathematical modeling of interleukin-27 induction of anti-tumor T cells response. *PLoS One* **9**, e91844; doi:10.1371/journal.pone.0091844 (2014).
10. Hilhorst, M., Shirai, T., Berry, G., Goronzy, J.J. & Weyand, C.M. T cell–macrophage interactions and granuloma formation in vasculitis. *Front.Immunol.* **5**, 432; doi: 10.3389/fimmu.2014.00432 (2014).
11. de Candia, P., Prattichizzo, F., Garavelli, S. & Matarese G. T Cells: warriors of SARS-CoV-2 infection, *Trends Immunol.* **42**, 18-30; <https://doi.org/10.1016/j.it.2020.11.002> (2021).
12. Oyler-Yaniv, A. *et al.* A tunable diffusion-consumption mechanism of cytokine propagation enables plasticity in cell-to-cell communication in the immune system, *Immunity* **46**, 609–620; doi:10.1016/j.immuni.2017.03.011 (2017).
13. Brocker, C., Thompson, D., Matsumoto, A., Nebert, D.W. & Vasiliou, V. Evolutionary divergence and functions of the human interleukin (IL) gene family. *Hum. Genomics* **5**, 30–55; doi: 10.1186/1479-7364-5-1-30 (2010).
14. Hesketh, M., Sahin, K.B., West, Z.E. & Murray, R.Z. Macrophage phenotypes regulate scar formation and chronic wound healing. *Int. J. Mol. Sci.* **18**, 1545-10; doi:10.3390/ijms18071545 (2017).
15. Nickaen, N., Ghaisari, J., Heiner, M., Moein, S. & Gheisari Y. Agent-based modeling and bifurcation analysis reveal mechanisms of macrophage polarization and phenotype pattern distribution. *Sci. Rep.* **9**, 12764; <https://doi.org/10.1038/s41598-019-48865-z> (2019).
16. Novak, M.L. & Koh, T.J. Macrophage phenotypes during tissue repair. *J. Leukoc. Biol.* **93**, 875-881; doi:10.1189/jlb.1012512 (2013).
17. Leonard, F. *et al.* Macrophage polarization contributes to the anti-tumoral efficacy of mesoporous nanovectors loaded with albumin-bound paclitaxel. *Front. Immunol.* **8**, 693; doi: 10.3389/fimmu.2017.00693 (2017).
18. Zhang, X. & Mosser, D.M. Macrophage activation by endogenous danger signals. *J. Pathol.* **214**, 161–178; doi:10.1002/path.2284 (2008).

19. Braune, J. *et al.* IL-6 regulates M2 polarization and local proliferation of adipose tissue macrophages in obesity. *J. Immunol.* **198**, 2927-2934; doi:10.4049/jimmunol.1600476 (2017).
20. Couper, K.N., Blount, D.G. & Riley, E.M. IL-10: the master regulator of immunity to infection. *J. Immunol.* **180**, 5771-5777; doi: 10.4049/jimmunol.180.9.5771 (2008).
21. Mahlbacher, G., Curtis, L.T., Lowengrub, J. & Frieboes, H.B. Mathematical modeling of tumor-associated macrophage interactions with the cancer microenvironment. *J. Immunother. Cancer* **6**, 10-17; doi 10.1186/s40425-017-0313-7 (2018).
22. Vianello, F., Olszak, I.T. & Poznansky, M.C. Fugetaxis: active movement of leukocytes away from a chemokinetic agent. *J. Mol. Med.* **83**, 752-763; doi: 10.1007/s00109-005-0675-z (2005).
23. Zitzmann, C. *et al.* A coupled mathematical model of the intracellular replication of dengue virus and the host cell immune response to infection. *Front. Microbiol.* **11**, 725; doi: 10.3389/fmicb.2020.00725 (2020).
24. Huang, C. *et al.* Clinical features of patients infected with 2019 novel coronavirus in Wuhan, China. *Lancet* **395**, 497-506; [https://doi.org/10.1016/S0140-6736\(20\)30183-5](https://doi.org/10.1016/S0140-6736(20)30183-5) (2020).
25. Zhou, F. *et al.* Clinical course and risk factors for mortality of adult inpatients with COVID-19 in Wuhan, China: a retrospective cohort study. *Lancet* **395**, 1054-62; [https://doi.org/10.1016/S0140-6736\(20\)30566-3](https://doi.org/10.1016/S0140-6736(20)30566-3) (2020).
26. Du, Y. *et al.* Cannabinoid 2 receptor attenuates inflammation during skin wound healing by inhibiting M1 macrophages rather than activating M2 macrophages. *J. Inflamm.* **15**, 25; <https://doi.org/10.1186/s12950-018-0201-z> (2018).
27. Longhi, M.P. *et al.* Interleukin-6 is crucial for recall of influenza-specific memory CD4⁺ T cells. *PLoS Pathog.* **4**, e1000006; doi:10.1371/journal.ppat.1000006 (2008).
28. Qi, F., Qian, S., Zhang, S. & Zhang Z. Single cell RNA sequencing of 13 human tissues identify cell types and receptors of human coronaviruses. *Biochem. Biophys. Res. Commun.* **526**, 135-140; <https://doi.org/10.1016/j.bbrc.2020.03.044> (2020).
29. Perelson, A.S., Kirschner, D.E. & De Boer R. Dynamics of HIV infection of CD4⁺ T cells. *Math. Biosci.* **114**, 81-125; doi: 10.1016/0025-5564(93)90043-a (1993).
30. Trinschek, B. *et al.* Kinetics of IL-6 production defines T effector cell responsiveness to regulatory T cells in multiple sclerosis. *PLoS One* **8**, e77634; doi:10.1371/journal.pone.0077634 (2013).
31. Li, B., Jones, L.L. & Geiger, T.L. IL-6 promotes T cell proliferation and expansion under inflammatory conditions in association with low-level ROR γ t expression. *J. Immunol.* **201**, 2934-2946; www.jimmunol.org/cgi/doi/10.4049/jimmunol.1800016 (2018).
32. Akdis, C.A. & Blaser, K. Mechanisms of interleukin-10-mediated immune suppression. *Immunology* **103**, 131-136 (2001).
33. Jankovic, D., Kugler, D.G. & Sher A. IL-10 production by CD4⁺ effector T cells: a mechanism for self-regulation. *Mucosal Immunol.* **3**, 239-246; doi: 10.1038/mi.2010.8 (2010).
34. Roberts, C.A., Dickinson, A.K. & Taams, L.S. The interplay between monocytes/macrophages and CD4⁺ T cell subsets in rheumatoid arthritis. *Front. Immunol.* **6**, 571; doi: 10.3389/fimmu.2015.00571 (2015).
35. Ross, E.A., Devitt, A. & Johnson, J.R. Macrophages: the good, the bad, and the gluttony. *Front. Immunol.* **12**, 708186; doi: 10.3389/fimmu.2021.708186 (2021).
36. Maneechotesuwan, K., Kasetsinsombat, K., Wamanuttajinda, V., Wongkajornsilp, A. & Barnes, P.J. Statins enhance the effects of corticosteroids on the balance between regulatory T cells and Th17 cells. *Clin. Exp. Allergy* **43**, 212-222; doi: 10.1111/cea.12067 (2013).
37. Miki, H., Pei, H., Gracias, D.T., Linden, J. & Croft M. Clearance of apoptotic cells by lung alveolar macrophages prevents development of house dust mite-induced asthmatic lung inflammation. *J. Allergy Clin. Immunol.* **147**, 1087-92.e3;

doi: 10.1016/j.jaci.2020.10.005 (2021).

38. Mannar, D., Leopold, K. & Subramaniam S. Glycan reactive anti-HIV-1 antibodies bind the SARS-CoV-2 spike protein but do not block viral entry. *Sci. Rep.* **11**, 12448-9; <https://doi.org/10.1038/s41598-021-91746-7> (2021).
39. Fardoos, R. *et al.* HIV infection drives interferon signaling within intestinal SARS-CoV-2 target cells. *JCI Insight* **6**, e148920; <https://doi.org/10.1172/jci.insight.148920> (2021).
40. Zhang, W. *et al.* The use of anti-inflammatory drugs in the treatment of people with severe coronavirus disease 2019 (COVID-19): the perspectives of clinical immunologists from China. *Cl. Imm.* **214**, 108393. <https://doi.org/10.1016/j.clim.2020.108393> (2020).
41. Brainard, D.M. *et al.* Migration of antigen-specific T cells away from CXCR4-binding human immunodeficiency virus type 1 gp120. *J. Virol.* **78**, 5184-5193; doi: 10.1128/JVI.78.10.5184-5193.2004 (2004).
42. Hadjadj, J. *et al.* Impaired type I interferon activity and inflammatory responses in severe COVID-19 patients *Science* **369**, 718-724; DOI:10.1126/science.abc6027 (2020).
43. Yang, L. *et al.* COVID-19: immunopathogenesis and immunotherapeutics, *Signal Transduction and Targeted Therapy* **5**,128; <https://doi.org/10.1038/s41392-020-00243-2> (2020).
44. Owen, M.R., Byrne, H.M. & Lewis, C.E. Mathematical modelling of the use of macrophages as vehicles for drug delivery to hypoxic tumour sites. *J. Theor. Biol.* **226**, 377-391; doi:10.1016/j.jtbi.2003.09.004 (2004).
45. Patra, T. *et al.* SARS-CoV-2 spike protein promotes IL-6 trans-signaling by activation of angiotensin II receptor signaling in epithelial cells. *PLoS Pathog.* **16**, e1009128; <https://doi.org/10.1371/journal.ppat.1009128> (2020).
46. Wager, C.M.L. & Wormley Jr F.L. Classical versus alternative macrophage activation: the Ying and the Yang in host defense against pulmonary fungal infections. *Mucosal Immunol.* **7**, 1023-1035; doi:10.1038/mi.2014.65 (2014).
47. Aste-Amezaga, M., Ma, X., Sartori, A. & Trinchieri, G. Molecular mechanisms of the induction of IL-12 and its inhibition by IL-10. *J. Immunol.* **160**, 5936-5944 (1998).
48. Zienkiewicz, O.C. & Taylor, R.L. *The Finite Element Method* (Butterworth-Heinemann, 2002).
49. Nicholls, J.M. *et al.* Lung pathology of fatal severe acute respiratory syndrome. *Lancet* **361**, 1773-78; doi: 10.1016/s0140-6736(03)13413-7 (2003).
50. Gu, J. *et al.* Multiple organ infection and the pathogenesis of SARS. *J. Experim. Med.* **202**, 415-424; www.jem.org/cgi/doi/10.1084/jem.20050828 (2005).
51. Ng, D.L. *et al.* Clinicopathologic, immunohistochemical, and ultrastructural findings of a fatal case of Middle East Respiratory Syndrome Coronavirus Infection in the United Arab Emirates, April 2014. *Am. J. Path.* **186**, 652-658; <http://dx.doi.org/10.1016/j.ajpath.2015.10.024> (2016).
52. Chistiakov, D.A., Killingsworth, M.C., Myasoedova, V.A., Orekhov, A.N. & Bobryshev Y.V. CD68/macrosialin: not just a histochemical marker. *Lab. Invest.* **97**, 4-13; doi: 10.1038/labinvest.2016.116 (2017).

Acknowledgements

Work carried out under the auspices of the INDAM-GNFM.

Additional Information

Supplementary information accompanies this paper.

Competing interests: The author declares no competing interests.

Figure legends

Figure 1. Snapshots of the virus density. Each panel is obtained at the indicated time steps and ϕ_{52} values. All the other parameters are as in Table 1. The density is linearly mapped in colour scale between the blue and red colours.

Figure 2. Snapshots of the T cells density. Each panel is obtained at the indicated time steps and ϕ_{52} values. All the other parameters are as in Table 1. The density is linearly mapped in colour scale between the blue and red colours.

Figure 3. Calculated amount of the simulated species present in the domain at each time step.

Figure 4. Cross-sectional densities for V , T and I cells. Each curve refers to the density at the pertinent time step obtained along the diagonal cut-line, see text for explanation.

Figure 5. Cross-sectional densities for $M1$ and $M2$ cells. Each curve refers to the density at the pertinent time step obtained along the diagonal cut-line, see text for explanation.

Figure 6. Cross-sectional densities for L and N cells. Each curve refers to the density at the pertinent time step obtained along the diagonal cut-line, see text for explanation.

Table legend

Table 1. Summary of the parameters and reference quantities used in the model.

Reference Quantity	Symbol	Units	Value
Virus (V)	V_r	N cm^{-3}	1×10^7
T cells	T_r	cell cm^{-3}	5×10^6
T maximum carrying capacity	T_M	cell cm^{-3}	5×10^6
I cells	I_r	cell cm^{-3}	5×10^6
M1 macrophages	MI_r	cell cm^{-3}	6.9×10^6
M1 maximum carrying capacity	MI_M	cell cm^{-3}	6.9×10^6
M2 macrophages	$M2_r$	cell cm^{-3}	6.9×10^6
IL-6 (L)	L_r	cell cm^{-3}	2.87×10^9
IL-10 (N)	N_r	cell cm^{-3}	2.87×10^9
Characteristic Length	L	cm	0.1
Characteristic Diffusion Coefficient	D	cm s^{-1}	1×10^{-6}
Time Scale	τ	s	1×10^4

Description	Symbol	Units	Non-Dimensional Parameter	Value
V diffusion coefficient	D_V	$\text{cm}^2 \text{s}^{-1}$	$D_V D^{-1}$	1×10^{-2}
T diffusion coefficient	D_T	$\text{cm}^2 \text{s}^{-1}$	$D_T D^{-1}$	5×10^{-3}
I diffusion coefficient	D_I	$\text{cm}^2 \text{s}^{-1}$	$D_I D^{-1}$	5×10^{-3}
MI diffusion coefficient	D_{MI}	$\text{cm}^2 \text{s}^{-1}$	$D_{MI} D^{-1}$	5×10^{-5}
$M2$ diffusion coefficient	D_{M2}	$\text{cm}^2 \text{s}^{-1}$	$D_{M2} D^{-1}$	5×10^{-5}
L diffusion coefficient	D_L	$\text{cm}^2 \text{s}^{-1}$	$D_L D^{-1}$	1.45×10^{-2}
N diffusion coefficient	D_N	$\text{cm}^2 \text{s}^{-1}$	$D_N D^{-1}$	1.45×10^{-2}
V production coefficient	p	s^{-1}	$p \tau L_r V_r^{-1}$	1.16×10^{-1}
V clearing coefficient	c	s^{-1}	$c \tau$	6.94×10^{-2}
I chemotactic coefficient	χ_I	$\text{cm}^5 \text{s}^{-1} \text{cell}^{-1}$	$\chi_I I_r D^{-1}$	0.001
V fugetactic coefficient	χ_V	$\text{cm}^5 \text{s}^{-1} \text{cell}^{-1}$	$\chi_V V_r D^{-1}$	0.05
T decay rate	d_T	s^{-1}	$d_T \tau$	0.02
T infection rate	k	$\text{cm}^3 \text{s}^{-1} \text{cell}^{-1}$	$k \tau V_r$	7.4×10^{-4}
T activation rate by L	ϕ_{21}	s^{-1}	$\phi_{21} \tau L_r T_r^{-1}$	11.5
T production rate by M1	ϕ_{22}	s^{-1}	$\phi_{22} \tau MI_r T_r^{-1}$	2.3×10^7
T inhibition rate by N	ϕ_{23}	s^{-1}	$\phi_{23} \tau N_r T_r^{-1}$	22.96
T inhibition rate by M2	ϕ_{24}	s^{-1}	$\phi_{24} \tau M2_r T_r^{-1}$	0.95×10^5
I decay rate	δ	s^{-1}	$\delta \tau$	0.02
I reduction rate by hyper-inflammation	ϕ_{32}	$\text{cm}^3 \text{s}^{-1} \text{cell}^{-1}$	$\phi_{32} \tau L_r$	10
MI production rate by L	ϕ_{41}	s^{-1}	$\phi_{41} \tau L_r MI_r^{-1}$	0.001
MI inhibition rate by N	ϕ_{42}	s^{-1}	$\phi_{42} \tau N_r MI_r^{-1}$	0.001
$M2$ promotion rate by N	ϕ_{51}	s^{-1}	$\phi_{51} \tau N_r M2_r^{-1}$	0.1
$M2$ inhibition rate by L	ϕ_{52}	s^{-1}	$\phi_{52} \tau L_r M2_r^{-1}$	0.001
L production rate by M1	ϕ_{61}	s^{-1}	$\phi_{61} \tau MI_r L_r^{-1}$	0.5
L inhibition rate by N	ϕ_{63}	s^{-1}	$\phi_{63} \tau N_r L_r^{-1}$	0.01
N production rate by M2	ϕ_{71}	s^{-1}	$\phi_{71} \tau M2_r N_r^{-1}$	0.1
N inhibition rate by L	ϕ_{73}	s^{-1}	$\phi_{73} \tau L_r N_r^{-1}$	9.26×10^{-5}

Figures

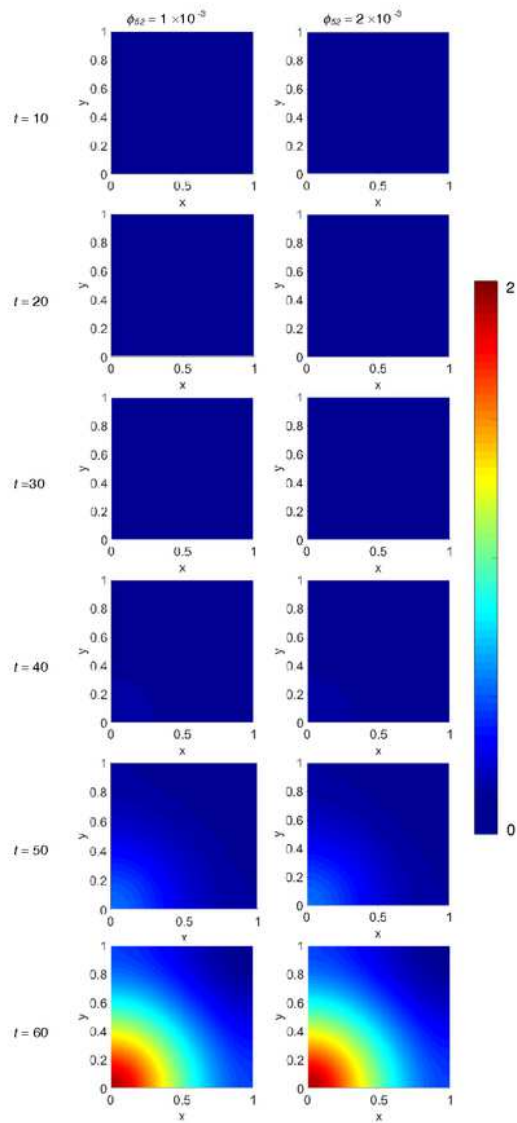


Fig. 1

Figure 1

Snapshots of the virus density. Each panel is obtained at the indicated time steps and Φ_{52} values. All the other parameters are as in Table 1. The density is linearly mapped in colour scale between the blue and red colours.

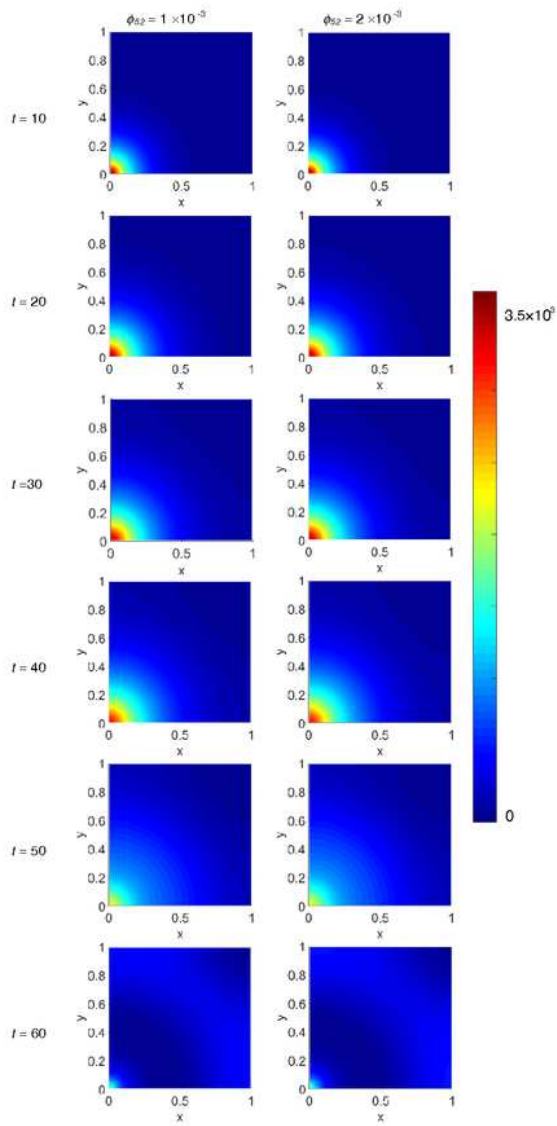


Fig. 2

Figure 2

Snapshots of the T cells density. Each panel is obtained at the indicated time steps and Φ_{52} values. All the other parameters are as in Table 1. The density is linearly mapped in colour scale between the blue and red colours.

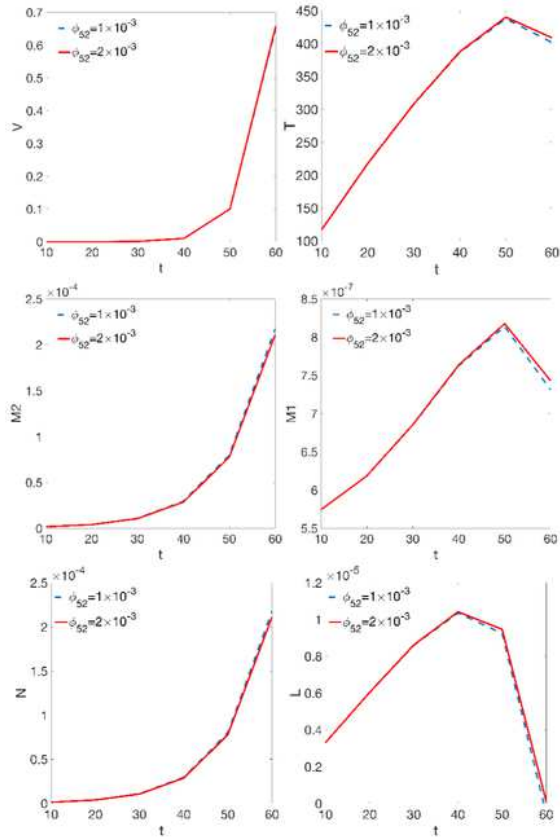


Fig. 3

Figure 3

Calculated amount of the simulated species present in the domain at each time step.

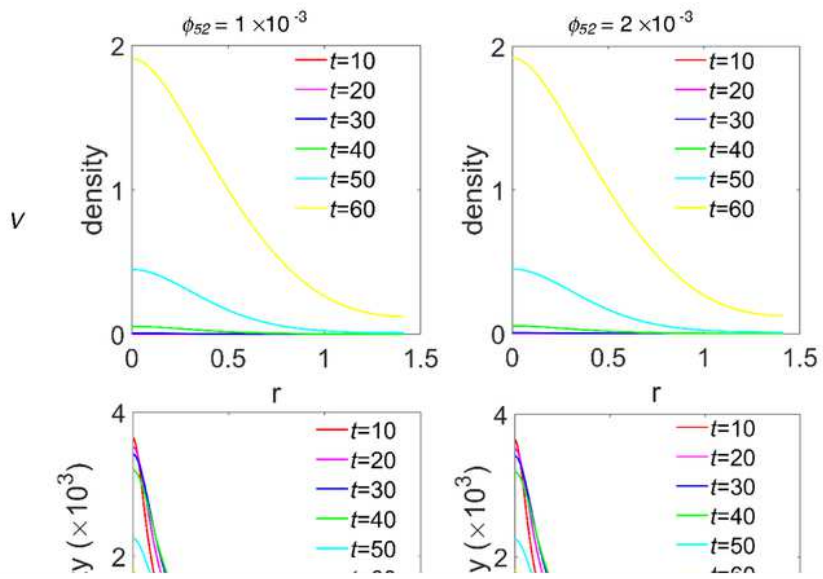


Figure 4

Cross-sectional densities for V, T and I cells. Each curve refers to the density at the pertinent time step obtained along the diagonal cut-line, see text for explanation.

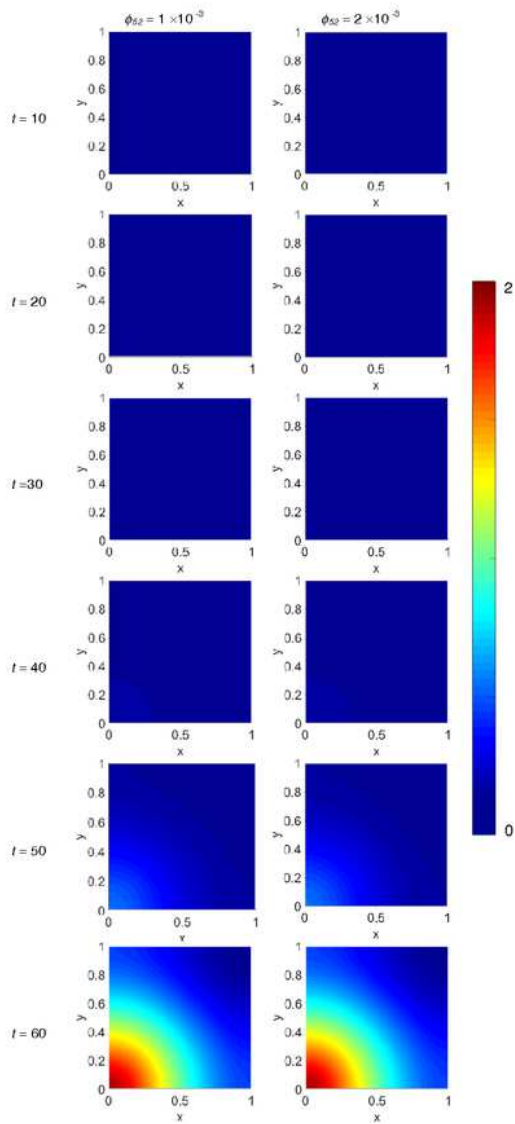


Fig. 1

Figure 5

Cross-sectional densities for M1 and M2 cells. Each curve refers to the density at the pertinent time step obtained along the diagonal cut-line, see text for explanation.

Figure 6

Cross-sectional densities for L and N cells. Each curve refers to the density at the pertinent time step obtained along the diagonal cut-line, see text for explanation.

Supplementary Files

This is a list of supplementary files associated with this preprint. Click to download.

- [TxtSubSuppl.pdf](#)